Master's Thesis

Characterization of filtered Cathodic Arc Plasma Processes

Focusing on Mass Spectroscopy and Ion Flux measurements

Investigation of correlation between ion flux and deposition rate for TiAl and TiAlN thin films

Author

Paul Junk

Supervisors

Dr. Yeliz Unutulmazsoy

Dr. Dmitry Kalanov

Institution

Leibniz Institute of Surface Engineering (IOM)

Leipzig University

Contents

Abstract

CHAPTER 1

Introduction

Theoretical Background

2.1 Plasma Generation and Composition

2.1.1 Cathode Spot Plasma Generation

Cathodic-arc plasmas are born in microscopic emission centers, so-called cathode spots, on an otherwise cold metal electrode under vacuum. A spot is ignited when the local cathode surface, often via a breakdown of adsorbates or field-enhanced thermionic emission, undergoes a rapid, explosive release of electrons and vaporized metal. During a single spot pulse, a few nanograms of the cathode material rapidly heat up, vaporize, and ionize, producing a dense, quasineutral plasma plume composed mostly of metal ions and electrons. The peak spot current densities reach 10^{10}–$10^{12}\,\mathrm{A\,m^{-2}}$, far above steady-state thermionic or field emission limits. These microexplosions, known as ectons (explosive electron emission centers), are characterized by localized, nanosecond-scale bursts of plasma and are sustained by repetitive ecton events at the same nominal location [2, Chap. 3.3–3.4].

Key Characteristics of Spot-Generated Plasma:

- High degree of ionization: >90 % of the ejected metal atoms emerge as ions, a consequence of the extreme power density in the cathode spot [2, Chap. 3.5].

- Multiply charged ions: the charge state distributions extend to $Q = 3$–4 for refractory metals, such as Ti and Al, due to the high electron temperature and density in the spot plasma [2, Chap. 3.5].

- Transient, localized heating: the sub-µm, sub-100 ns pulse produces "atomic-scale heating", where the energy of individual ions is deposited in a highly localized region upon impact, influencing film growth and microstructure [2, Chap. 3.6].

Spot ignition and quenching occur on the order of 10–100 ns, with each pulse launching a fully ionized slug of metal vapour. The sustained arc discharge therefore comprises a continual overlap of these microplasma bursts, producing a metal-rich, high-flux ion stream ideal for energetic thin-film growth.

2.1.2 Plasma Composition and Expansion

Once generated at the cathode spots, the metal-rich plasma expands into the chamber or through the magnetic macroparticle filter. In the region near the cathode (within a few centimeters of the spot), plasma densities are on the order of 10^{18} cm^{-3} and electron temperatures $T_e \approx 5 - 10$ eV. As the plume propagates, its density decreases according to

$$n(r) = \frac{C\, I_{\mathrm{arc}}}{r^2} \tag{2.1}$$

where I_{arc} is the arc current r the distance, and C a constant related to the ion-erosion rate of the cathode material. This $\frac{1}{r^2}$ scaling assumes free expansion, but deviations can occur due to magnetic fields, collisions, or reactive gases, which may alter the plasma trajectory or cause recombination [2, Chap. 4.3; Eq. 4.3, p. 178].

In cathodic-arc discharges from titanium cathodes, whether pure Ti or Ti–Al compounds, ions generally carry an average charge state $\langle Q \rangle \approx$ 2.1–2.2 [2, Chap. 4.1; App. B.8]. This high degree of ionization reflects the extreme power density of the spot and follows the cohesive energy rule, which links $\langle Q \rangle$ to the cohesive energy of the cathode material (Table B.8) [2, App. B.8].

2.2 Ion Energy and Flux

2.2.1 Ion Energies: Origins and Implications

Ion energies in cathodic arc plasmas are well-documented, with Ti^{2+} and Al^{2+} ions carrying kinetic energies of $E_{kin}^{\mathrm{Ti}^{2+}} \approx 58.9$ eV and $E_{kin}^{\mathrm{Al}^{2+}} \approx 27.5$ eV, respectively [2, Chap. 4.4; Table B.8]. Combined with potential energy from ionization, these ions reach total energies ($E_{tot}^{\mathrm{Ti}^{2+}} \approx 79.5$ eV, $E_{tot}^{\mathrm{Al}^{2+}} \approx 52.0$ eV) that exceed the ≈ 30 eV threshold for subplantation, enabling densification and crystallinity in Ti–Al–N films [2, Chap. 8.1–8.2].

While ion energies contribute to film properties, this work prioritizes quantifying the flux of excited nitrogen species alongside metal ions to understand their combined role in film growth and densification.

In metallic mode, the narrow ion energy distribution simplifies flux measurements, allowing direct correlation with deposition outcomes.

In reactive mode, collisions with N_2 not only broaden the energy distribution but also generate excited nitrogen (e.g., N^+, N_2^+, and metastable neutrals), which must be resolved in QMS spectra [5].

To isolate the effects of ion flux (Γ) and excited nitrogen, we systematically vary the N_2 pressure over a wide range and adjust the field strength of the EM coil, ensuring that changes in film properties reflect controlled variations in plasma composition and flux rather than incidental energy shifts.

2.2.2 Ion Flux and Diagnostics

The ion flux, Γ (ions·cm^{-2}·s^{-1}), represents the number of ions impinging per unit area per unit time. In a multiply charged plasma, the total measured ion current density J_i (A·cm^{-2}) relates to Γ via:

$$\Gamma = \frac{J_i}{e \langle Q \rangle}. \tag{2.2}$$

This relationship is central to our experiments, as the time-averaged ion flux Γ is expected to correlate with the total deposited mass measured by the QCM (Section 3.2.2).

To compare ion fluxes across different materials and arc currents, we use the particle system coefficient:

$$k_{\mathrm{part}} = \frac{I_i}{\langle Q \rangle \, I_{\mathrm{arc}}}, \tag{2.3}$$

which normalizes the probe current I_i by the arc current I_{arc} and accounts for variations in the average charge state $\langle Q \rangle$ [2, Chap. 6.5]. An external magnetic field can increase Γ by up to an order of magnitude by confining the plasma and prolonging the ion residence time near the cathode [2, Chap. 6.5]. This enhancement is particularly relevant for our study, where magnetic fields are used to tune plasma properties and investigate their influence on the deposited mass.

In vacuum cathodic arcs, the burning voltage remains nearly constant at 20–30 V for arc currents up to 1 kA, so the plasma generation rate - and thus Γ - increases

almost linearly with I_{arc} [2, Chap. 6.5]. Introducing source modifications, such as an external magnetic coil, increases the spot power density and prolongs the plasma residence time at the cathode, further increasing the total ion flux by up to an order of magnitude.

To link ion arrival with film growth, we mounted a QCM adjacent to the ion probe. Each ion that sticks to the crystal shifts its resonance frequency by Δf. Using the Sauerbrey equation, we convert Δf into a mass flux $\dot{m}$ and then divide by the density of the film ρ_{film} to obtain the thickness growth rate:

$$R = \frac{\dot{m}}{\rho_{\text{film}}} = \frac{m_{\text{ion}} \, \Gamma \, S}{\rho_{\text{film}}}, \tag{2.4}$$

where m_{ion} is the mass of an ion, Γ the ion flux measured by the probe, S the sticking coefficient (≈ 1), and ρ_{film} the density of the film.

In previous research by Unutulmazsoy et al. (2023), when ion energy is fixed, R rises almost linearly with Γ. Any deviation from this linear behavior signals that other processes, such as densification or adatom crowding, are beginning to influence film growth [25].

To connect the theory of ion flux and energy to experimental data, we employ two primary diagnostics:

- A current-density probe to record the time-resolved ion current $I_i(t)$, from which we compute the flux $\Gamma(t) = \frac{I_i(t)}{(e\langle Q \rangle)}$.

- A quadrupole mass spectrometer (QMS) to resolve the ion-energy distribution (IEDF) and charge-state spectrum, yielding E_{kin} and $\langle Q \rangle$.

Together, these tools let us map how variations in Γ, E_{kin} and $\langle Q \rangle$ translate into film growth. The detailed design of the probe, the geometry of the QMS orifice, the calibration procedures, and the data acquisition settings are described in Chapter 3.2.4.

2.3 Plasma-Surface Interactions and Film Growth

2.3.1 Energetic Condensation and Subplantation

When energetic metal ions strike the growing film, they can penetrate the surface and deposit their energy in a shallow 'collision cascade'. This subplantation process leads to two key effects:

- **Localized densification**:
  Ions with kinetic energies above the $\approx$ 20–30 eV threshold implant beneath the growing surface, filling interstitial sites and displacing adatoms via knock-on collisions. This process reduces porosity and increases the density of the film, which is particularly critical for Ti–Al–N coatings [2, Chap. 8.1].

- **Atomic-scale heating**:
  The deposition of kinetic energy and the release of potential energy (ionization enthalpy) generate localized, nanosecond-scale temperature spikes, enhancing adatom mobility and promoting crystallite coalescence without global substrate heating [2, Chap. 8.2].

As E_{kin} and E_{pot} increase, transition from porous, amorphous structures to dense, crystalline coatings with compressive stresses of several GPa, driven by atomic peening [2, Chap. 8.1–8.4]. For example, TiN films grown with $E_{\text{kin}} \approx 40$ eV and $E_{\text{pot}} \approx 20$ eV develop a preferred cubic (111) texture and hardness > 30 GPa.

In this work, we systematically investigate how controlling E_{kin}, E_{pot} (Section **??**), and tuning the ion flux Γ (Section **??**) influence densification, texture evolution, and stress development in Ti–Al–N coatings. The results are presented in Chapter **??**.

2.3.2 Reactive vs Metallic Mode

Cathodic-arc deposition can operate in two distinct regimes: metallic mode and reactive mode. In metallic mode, the cathode surface remains uncovered, and the plasma consists exclusively of metal ions. This regime is characterized by a stable burning voltage, minimal macroparticle emission, and a high metal ion flux. In reactive mode, a background gas (e.g., N_2) adsorbs onto the cathode surface, forming a compound layer that 'poisons' the cathode. This alters both the behaviour of the cathode spot and the composition of the plasma [2, Chap. 9.2].

When N_2 is introduced, a dynamic equilibrium forms between compound formation (adsorption and reaction at the cathode, which suppresses metal emission) and compound removal (via explosive ecton events that clean the spot and eject both metal and compound fragments) [2, Chap. 9.3].

The equilibrium position depends on gas pressure, arc current, and cathode composition. At low N_2 pressures or high power densities, type-2 (metal-rich) spots prevail, maintaining a predominantly metal ion flux. At higher pressures or for larger cathode areas, type-1 (poisoned) spots dominate, producing a mixed plasma of metal and N_x ions while suppressing macroparticle emission [2, Chap. 9.4]. This poisoning effect is

reversible and depends on the balance between compound formation and ecton-induced cleaning [2, Chap. 9.3].

Reactive mode affects both plasma diagnostics and film growth:

- The probe current includes contributions from N^+ and N_2^+ ions in addition to metal ions, necessitating mass-resolved QMS analysis to distinguish between species [5].

- Charge exchange with N_2 reduces the average charge state of metal ions (Q) and introduces additional gas ion charge states, altering the overall potential energy budget [2, Chap. 9.4].

- Collisions between ions and N_2 molecules during plasma expansion lower ion drift velocities, thereby reducing their kinetic energy before substrate impact [2, Chap. 9.4].

In our Pi-PVD system, N_2 is introduced via a ring-manifold inlet located downstream of the magnetic filter, minimizing pressure gradients and enabling reproducible reactive mode operation. By comparing depositions in vacuum and under varying N_2 concentrations, we investigate how reactive mode influences Γ, E_{kin}, and Q, and how these parameters affect the deposited mass (measured by QCM) and the resulting film microstructure (Chapter **??**).

2.4 Crystal Structure and Densification

2.4.1 Nucleation and Growth Modes

Experimental Methodology

3.1 Experimental Apparatus and Setup

3.1.1 Vacuum & Gas Infrastructure

The chamber was evacuated using a two-stage pumping system consisting of a turbo-molecular pump (backed by a rotary vane pump for initial roughing) and a cryogenic pump, achieving a base pressure of 1×10^{-5} Pa. Nitrogen gas (N_2, 99.999% purity) was introduced via a mass flow controller (MFC), with chamber pressures ranging from 0.025–0.3 Pa during experiments,

Plasma was generated using a water-cooled cathode composed of 75 wt% Ti–25 wt% Al (62.8 at% Ti–37.2 at% Al) with a diameter of 6.35 mm and 38.1 mm long. The arc power supply operated in pulsed DC mode, delivering up to 450 A at a pulse frequency of 0.2–5 Hz, and also powered the 90° curved macroparticle filter in series. An accelerator coil (EM-coil), capable of currents up to 850 A, was pulsed 200 μs before arc ignition to stabilize the magnetic field. The QCM and Langmuir probe were mounted on a custom adjustable mechanism screwed to the chamber floor at 10–20 cm from the filter exit, while the energy-resolving mass spectrometer (ERMS) was positioned using a linear feedthrough for external adjustment.

The vacuum chamber setup for cathodic arc plasma diagnostics and thin film deposition is shown in Figure 3.1. The arc power supply generates and steers the plasma, while the EM-coil power supply enhances the plasma energy and confinement.

The green arrow illustrates the trajectory of the plasma plume as it expands from the cathode, passes through the macroparticle filter, and reaches the diagnostics. An energy-resolving mass spectrometer (ERMS) analyzes the ion energy and mass distribution, with its position adjusted relative to the macroparticle filter, to study spatial variations in the plasma plume. A Langmuir probe measures the ion current, and a quartz crystal microbalance (QCM) monitors the deposited mass in situ. An oscilloscope records time-resolved electrical signals: channels 1 and 2 measure the voltage drop at the cathode, while channels 3 and 4 capture the current supplied to the arc and EM-coil, as well as the ion current collected by the probe on another channel. The delay generator acts as a master clock, triggering the arc power supply, EM-coil activation, and diagnostic tools with precise timing to ensure that ion flux, energy, and deposition rate measurements are directly comparable and time-correlated.
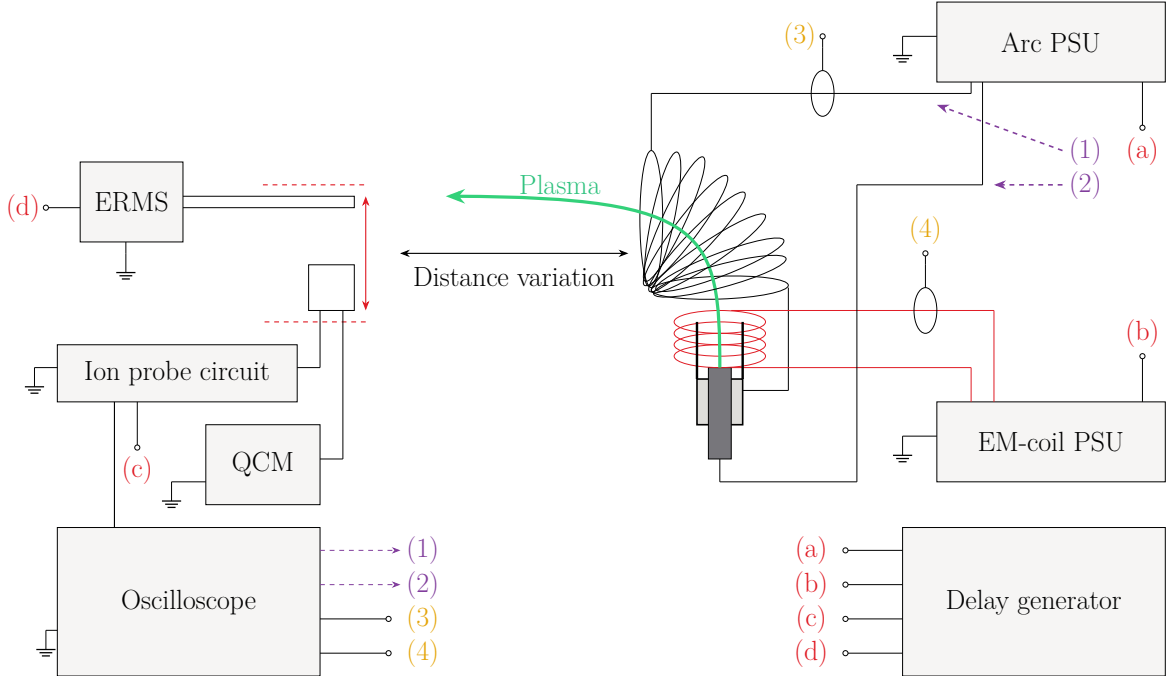
Figure 3.1: Schematic of the vacuum chamber setup for cathodic arc plasma diagnostics and thin film deposition. (a) Arc power supply, (b) EM-coil power supply, (c) Langmuir probe and QCM, (d) energy-resolving mass spectrometer (ERMS). The delay generator (a–d) synchronizes the arc power supply, EM-coil activation, and diagnostic tools.

3.1.2   Power & Triggering

The arc power supply operated in pulsed mode at a frequencies between 0.2–5 Hz with a pulse width of 1 ms. The EM-coil was activated 200 μs before arc ignition and lasts 1.5 ms, to ensure steady-state magnetic field conditions. A delay generator (SRS DG645) served as the master clock, distributing triggers to:

- the arc power supply (channel **a**),

13

- the EM-coil power supply (channel **b**),
- the diagnostics (ERMS, QCM, and Langmuir probe; channels **c**–**d**).
- the oscilloscope is triggered on the rising edge of the arc power supply unit (PSU) voltage (Channel (1))

This setup enabled time-resolved measurements of ion flux and energy, fully synchronized with plasma generation.
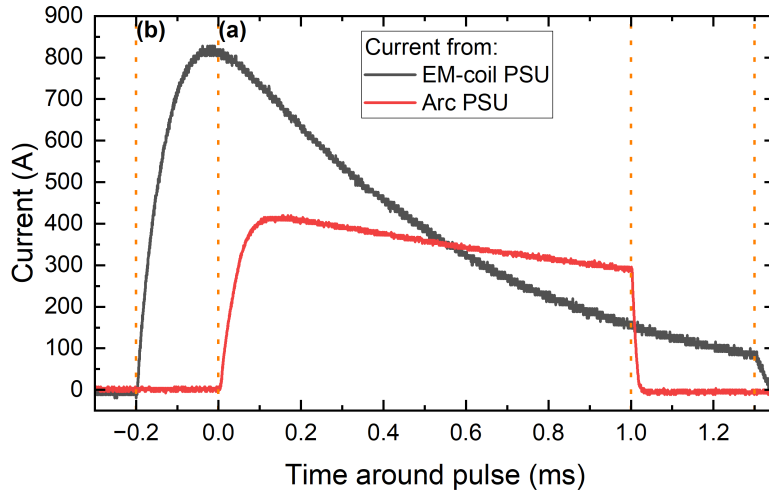
Figure 3.2: Example Pulse waveform with the triggering timings (a) and (b) for the Arc-PSU and the EM-coil PSU marked with the orange dashed line

To approximate the magnetic field generated within the EM-coil solenoid, the following equation was utilized:

$$B = \frac{\mu_0 N I}{L} \tag{3.1}$$

with the length of the solenoid $L = 0.02m$, the number of turns in the solenoid $N = 5$ and the vacuum permeability $\mu_0 = 1.256 \cdot 10^{-6} \frac{T \cdot m}{A}$. The electrical current value was determined by the peak current recorded with the oscilloscope, typically observed around the 0 ms point, as illustrated in Fig. 3.2. This approach was adopted because the shape of the current curve varies significantly depending on the input voltage and the resulting current. Figure 3.2 depicts the current curve achieved for a 250V input. Additionally the current curve for a 100V input is provided in the Appendix (Fig. A.1).

14

3.2   In situ Diagnostics

3.2.1   Ion-current Probe- Langmuir probe

The in-house-built ion collector probe (Figure 3.3) was designed to measure the current density of ions (J_i) in ion saturation mode. The probe consisted of a 5 mm diameter copper stick milled down to resemble a nail, it was then covered with Katpon tape to ensure insulation from the holder assembly 3.6.
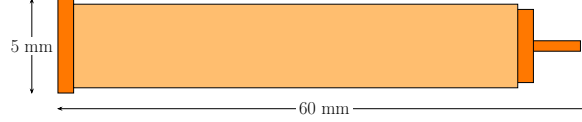

Figure 3.3: In-house built ion collector probe wrapped in Kapton tape for electrical insulation from the aluminum assembly holder. The probe includes an attachment point for a screw terminal connector, enabling connection to the ion probe circuit (Figure 3.4)

To guarantee full ion collection, the probe was negatively biased at $V_b = -80$ V. The measured voltage (V_m) was corrected for the voltage divider effect introduced by the 1 kΩ bias resistor, using the following relationship:

$$V_{\text{true}} = \frac{1000 + 400 \ \Omega}{1000 \ \Omega} \cdot V_m = 1.4 \cdot V_m. \tag{3.2}$$
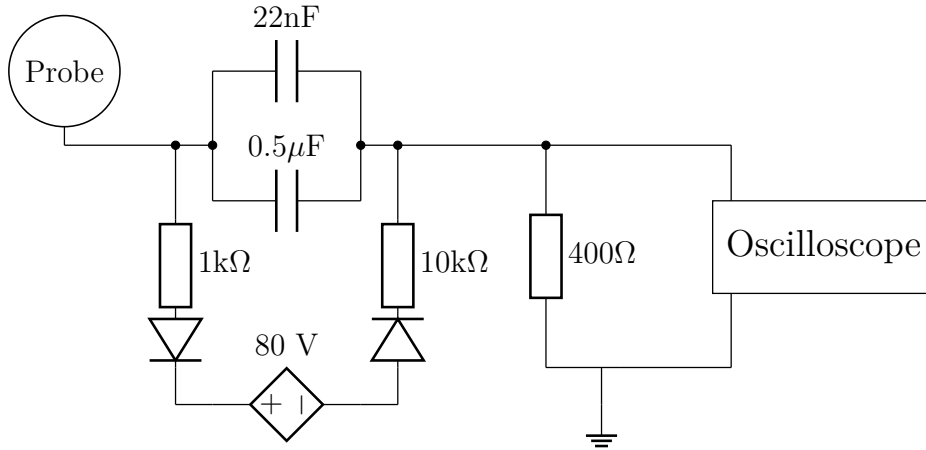
Figure 3.4: Schematic of the ion-flux probe circuit. The $400\,\Omega$ resistor converts ion current to voltage, while the $0.5\,\mu\text{F}$ capacitor and $400\,\Omega$ resistor form a high-pass filter with a $795\,\text{Hz}$ cutoff.

The circuit incorporates a $0.5\,\mu\text{F}$ capacitor in series with the $400\,\Omega$ resistor, forming a high-pass filter with a cutoff frequency of $795\,\text{Hz}$. This configuration effectively blocks DC and low-frequency noise, ensuring that only plasma fluctuations above $795\,\text{Hz}$ are recorded. The high-pass characteristic is essential for isolating the dynamic ion current

signal from any static offsets or drift.

To maintain a stable bias voltage, a $22\,\mathrm{nF}$ capacitor and $1\,\mathrm{k\Omega}$ resistor are included in the bias supply line. This combination acts as a low-pass filter, smoothing the bias voltage and minimizing high-frequency ripple.

The processed voltage signal is recorded using a 20 MHz bandwidth oscilloscope. The ion flux Γ_i is then calculated from the corrected voltage V_{true} as:

$$\Gamma_i = \frac{V_{\mathrm{true}}}{eAR}, \tag{3.3}$$

where $A = 19.63\,\mathrm{mm^2}$ is the probe area, e is the elementary charge, and $R = 400\,\Omega$. This setup ensures accurate measurement of the ion flux while minimizing the impact of noise and DC offsets.

3.2.2 Quartz Crystal Microbalance

A quartz crystal microbalance (QCM) was employed to measure the amount of material deposited during cathodic arc sputtering. The configuration used in this work was the INFICON Cool Drawer™ with a single drawer in standard orientation. The sensor is water-cooled to ensure thermal stability, and a 14 mm diameter, 6 MHz AT-cut quartz crystal was operated with a SQM-160 controller for electronic readout.
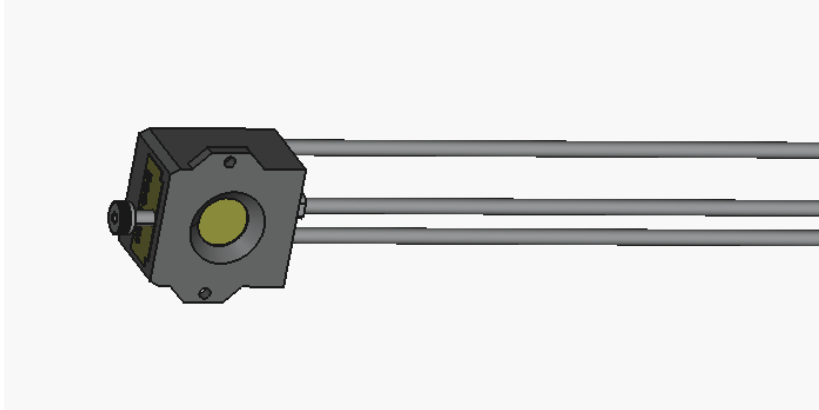
Figure 3.5: Sensor head of the INFICON Cool Drawer™ Quartz Crystal Microbalance (QCM) used for in-situ mass deposition monitoring during cathodic arc sputtering. The assembly includes a water-cooled housing, a 14 mm diameter AT-cut quartz crystal (6 MHz), and electrode leads for connection to the SQM-160 controller. (Schematic adapted from INFICON STP file, available at https://www.inficon.com/en/products/thin-film-technology/cool-drawer-single-sensor).

The measurement principle follows the Sauerbrey equation [22], which relates the change in resonance frequency of the quartz crystal to the deposited mass:

$$m = \frac{N_{\text{AT}} \cdot d_q \cdot \pi r^2}{F_q^2} \cdot \Delta F_c = 18.8146023 \cdot 10^{-9} \frac{g}{Hz} \cdot \Delta F. \tag{3.4}$$

Here $d_q = 2.649 \frac{\text{g}}{\text{cm}^3}$ is the quartz density, $N_{\text{AT}} = 166\,100\,\text{Hz cm}$ the frequency constant of the AT-cut, $F_q = 6\,\text{MHz}$ the uncoated resonance frequency, and ΔF the measured frequency shift.

The Sauerbrey relation is accurate as long as $\Delta F \lesssim 0.05 F_q$ (about $0.3\,\text{MHz}$ for a 6 MHz crystal). For larger mass loadings, the linear approximation fails and the Z-match™ technique is used. This method, introduced by Lu and Lewis in 1972 on the basis of Miller and Bolef's theoretical treatment [18, 16], incorporates the acoustic properties of both the quartz and the deposited film via the acoustic impedance ratio

$$Z = \left(\frac{d_q\,\mu_q}{d_f\,\mu_f} \right)^{1/2}, \tag{3.5}$$

with d and μ denoting the density and shear modulus of quartz (q) and film (f), respectively [14]. In practice, the controller applies a correction function $f(Z)$ to the Sauerbrey relation,

$$m_f = \frac{N_{\text{AT}}\,d_q\,\pi r^2}{F_q^2} \cdot \Delta F \cdot f(Z), \tag{3.6}$$

which compensates for the acoustic mismatch and extends the validity of thickness determination up to $\sim 0.4 F_q$.

In the present experiments, the observed frequency shifts ranged from about $1\,\text{Hz}$ to $50\,\text{Hz}$. With the SQM-160 resolution of approximately $0.03\,\text{Hz}$ at $6\,\text{MHz}$, even the smallest shifts were well above the noise floor, yet orders of magnitude below the Sauerbrey breakdown limit. The Sauerbrey approximation was therefore fully sufficient, and Z-match corrections were not required.

3.2.3 Comparability with QCM Measurements

The ion collector probe, with its 5 mm diameter, was mounted through a precision-milled pass-through hole in the aluminum mounting block, while the QCM was secured in a dedicated cutout and fixed via screws.

This configuration ensured rigid mechanical alignment between the two diagnostics. The exposed area of the quartz crystal (8 mm diameter) was selected to encompass the probe's collection area, enabling spatially resolved comparisons of ion current density and deposited mass.
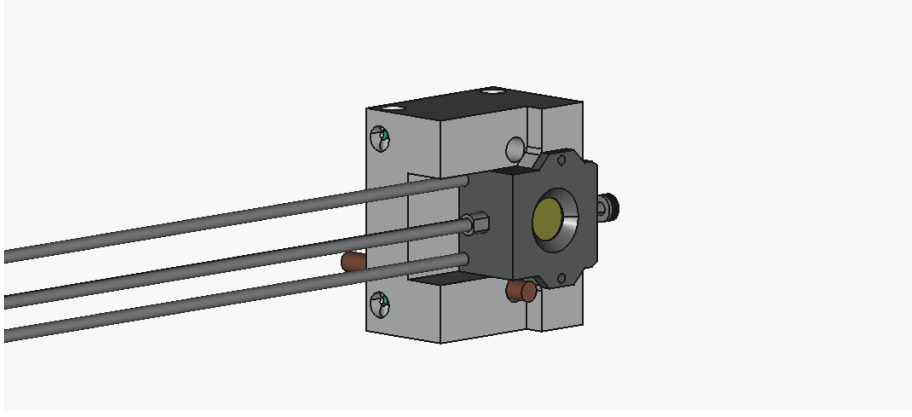
Figure 3.6: Holder Assembly for In-Situ Plasma Diagnostics: Integrated QCMs and Langmuir Ion Collector Probe (interactive 3D model; static preview shown in non-Adobe viewers).

This design accounts for the radial gradients in plasma density and ion charge state distribution, which are inherent to expanding cathodic arc plasmas [2, Chap. 6.2]. By positioning the probe right next to the QCM, the ion flux measurements directly reflect the plasma conditions governing deposition on the crystal surface.

3.2.4 Quadrupole Mass Spectrometer

A quadrupole mass spectrometer (QMS, Hiden EQP 1000) was used to measure the ion energy distribution functions (IEDFs) and charge-state-resolved fluxes of plasma species generated during pulsed cathodic arc deposition. The system combines an electrostatic energy analyzer with a quadrupole mass filter to separate ions by their kinetic energy and mass-to-charge ratio (m/q).

Ions enter the QMS through a $50\,\mu\mathrm{m}$ sampling orifice and are first transported to the energy analyzer, where their kinetic energy E_i is selected according to the relationship:

$$E_i = \left(V_{\mathrm{ENERGY}} + \frac{R}{d} V_{\mathrm{PLATES}} - V_{\mathrm{AXIS}} \right) n \times e. \tag{3.7}$$

Here, V_{ENERGY} and V_{AXIS} are opposing potentials applied to the analyzer, R is the mean radius of the cylindrical sector, d is the plate separation, V_{PLATES} is the potential difference across the sector plates, and $n \times e$ is the total charge of the ion [11]. The selected ions are then injected into the quadrupole mass filter, where a combination of AC and DC electric fields creates a stability region dependent on m/q, described by the Mathieu equations [9]. Only ions with trajectories stable in both radial and axial directions reach the detector. The potential in the quadrupole is described by:

$$V(x, y, t) = \frac{U_0 \cos(\omega t)}{r_0^2} (x^2 - y^2), \tag{3.8}$$

where U_0 is the amplitude of the AC voltage, ω is the angular frequency, and r_0 is the field radius. The stability of ion motion is determined by the dimensionless parameters:

$$a = \frac{8eU_{\mathrm{DC}}}{mr_0^2\omega^2}, \quad q = \frac{4eU_0}{mr_0^2\omega^2}, \tag{3.9}$$

with U_{DC} as the superimposed DC voltage. For a given m/q, stable transmission occurs only within specific (a, q) regions, enabling mass separation [9, 17].
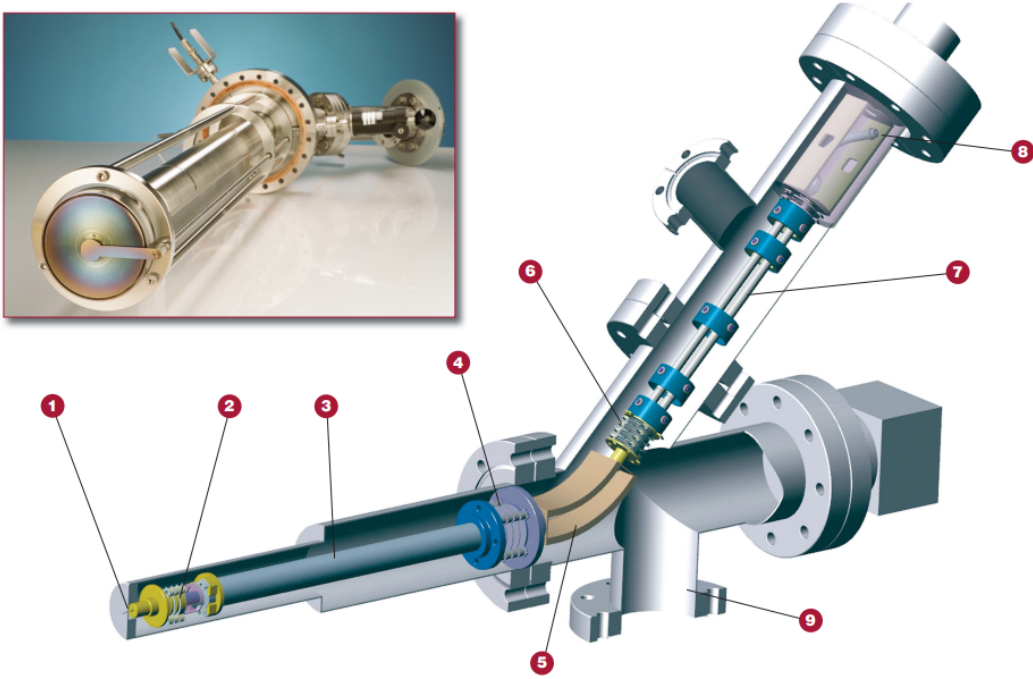

Figure 3.7: ERMS, Hiden EQP HE 1000: (1) Sampling Orifice, (2) Electron Impact Ion Source, (3) Transfer Ion Optics, (4) Quadrupole Lens, (5) Energy Filter, (6) Decelerating Lens, (7) Quadrupole Mass Filter, (8) Detector, (9) Differential Pump Port [1]

To obtain the ion energy distribution functions (IEDFs), the energy-to-charge (E/Q) distributions were measured for different mass-to-charge ratios (M/Q). The energy distributions for ions of different charge states were derived by multiplying the E/Q values by the corresponding charge state number Q. This correction accounts for the charge-dependent scaling of ion energies.

To reduce interference from the arc's magnetic field, the QMS was equipped with a grounded, mu-metal shield [4].

IEDFs were measured using a double trigger acquisition scheme synchronized with the arc pulses, which had a 1 ms duration and a 5 Hz repetition rate. For each m/q value, two 20 ms acquisition windows were recorded, activated 10 ms before the onset of

the pulse. The combined 40 ms of data for each point were averaged to obtain the final IEDF. Measurements were performed for charge states 1^+, 2^+, and 3^+ of aluminum ions, and for charge states 1^+, 2^+, 3^+, and 4^+ of titanium ions. For nitrogen ion species (N and N_2), only the 1^+ ionization level was measured. This was achieved by scanning V_{ENERGY} while fixing the quadrupole mass filter to the corresponding m/q values.

	Molar mass over charge ratio of:			
Ionization	Al	Ti	N	N_2
1+	27	47.867	14	28
2+	13.5	23.933	-	-
3+	9	15.955	-	-
4+	-	11.966	-	-

3.3 Ex situ Measurements

3.3.1 X-ray Diffraction (XRD)

X-ray diffraction (XRD) was employed to analyze the crystallographic structure of the thin films deposited during the experiments. XRD is a non-destructive technique that provides detailed information about the crystalline phases present in the material, as well as their lattice parameters, crystallite size, and strain.

The XRD measurements were performed using a [specific model, e.g., Bruker D8 Advance] diffractometer equipped with a Cu K_α radiation source ($\lambda = 1.5406$ Å). The diffractometer was configured with a [specific type of detector, e.g., scintillation counter] and a goniometer for precise angle measurements. The samples were mounted on a [specific type of sample holder, if applicable] and scanned over a 2θ range of [specific range, e.g., 20° to 80°] with a scan speed of [specific speed, e.g., 0.02° per second].

The crystallographic structure of the films was determined by analyzing the diffraction patterns obtained. The Bragg equation was used to identify the crystalline phases:

$$2d\sin(\theta) = n\lambda \tag{3.10}$$

where d is the spacing between atomic planes, θ is the angle of incidence, n is an integer, and λ is the wavelength of the X-rays.

The XRD data were processed using [specific software, e.g., Bruker DIFFRAC.SUITE] to identify the crystalline phases and determine their lattice parameters. The crystallite

size was estimated using the Scherrer equation:

$$\tau = \frac{K\lambda}{\beta \cos(\theta)} \tag{3.11}$$

where τ is the mean size of the crystalline domains, K is a dimensionless shape factor (typically 0.9), λ is the X-ray wavelength, β is the line broadening at half the maximum intensity (FWHM), and θ is the Bragg angle.

The XRD measurements were calibrated using a standard reference material (e.g., silicon powder) to ensure accuracy and reproducibility. The samples were prepared by [specific preparation method, e.g., cutting and polishing] to ensure a flat and representative surface for analysis.

3.3.2 X-ray Reflectometry (XRR)

3.3.3 Scanning Electron Microscopy (SEM)

3.3.4 Profilometry

Stylus profilometry was used to measure film thickness by mechanically tracing the surface topography using a diamond-tipped stylus. The technique provides direct measurement of step heights between masked and deposited regions, making it particularly useful for verifying film thickness values obtained by QCM [20].

In profilometry, a stylus with a small tip radius (typically 2–12 μm) is dragged across the sample surface with a controlled force (here 3 mg) while its vertical displacement is monitored electromagnetically. The resulting trace provides a profile of the surface from which the step height (film thickness) with vertical resolution down to $\sim$1 nm can be extracted.

The Dektak stylus profilometer used in this study has a measurement range from 6.5 nm to 800 μm with repeatability of 0.4 nm. For thickness measurements, silicon substrates were partially masked with a marker line, which created a well-defined step edge during deposition. This marker line was subsequently removed with Isopropanol in a ultrasonic bath. Multiple scans across each step were performed to ensure reproducibility, and the average thickness was calculated from at least three different positions on each sample.

One limitation of contact profilometry is the potential for stylus-induced damage on very soft films, though this was not a concern for the hard TiAlN coatings investigated here. The technique is complementary to XRR, with profilometry providing rapid,

direct thickness measurements while XRR offers higher accuracy for very thin films and additional information on density and roughness [27].

3.4 Data Processing

Experimental data were processed using custom Python scripts to ensure consistency and reproducibility. A central Excel logbook served as the reference for all measurements, each identified by a unique suffix and linked to its corresponding data files. The logbook recorded experimental parameters such as date, distance, pressures, MFC flow rate, cryopump position, power supply settings, and pulse characteristics, as well as initial and final QCM frequencies for deposited mass determination. Associated oscilloscope waveforms were stored as CSV files for ion current analysis.

A Python script automated data handling by matching logbook entries to raw data, averaging ion current waveforms over multiple pulses to reduce noise when possible, and compiling all parameters into a unified dataset. This ensured uniform processing and efficient preparation for subsequent analysis.

QMS data were evaluated with a separate Python script that integrated raw spectra, applied mass transmission corrections to account for detection biases, and extracted parameters such as mean ion energy, charge state distribution, and potential and kinetic energy components for each species (different ionization levels of the four atoms measured). The processed results were visualized and exported into a structured CSV file for detailed examination of the ion energy distributions.

3.5 Error Handling

3.5.1 Mass Spectrometry Measurements

In mass spectrometry measurements, particularly in the context of cathodic arc processes, the standard deviation is crucial for characterizing data variability. The non-stationary nature of cathode spots in cathodic arcs leads to significant fluctuations in ion flux and charge composition from pulse to pulse [2]. Calibrating mass spectrometry measurements can be challenging due to these fluctuations, as random errors at each standard point used to determine the calibration curve can lead to a distribution of values for the same observed response for the unknown [13]. As a result, achieving optimal calibration in such conditions may not be straightforward, and the accuracy of the calibration could be affected.

In this study, while efforts were made to calibrate the mass spectrometer accurately,

the inherent difficulties associated with the calibration process in cathodic arc environments suggest that the calibration might not have been optimal. To account for this potential source of error, the impact of truncating the measurement artifact (e.g., signal noise or background interference) at different points was evaluated, and its effect on the data was analyzed in detail. This analysis will be further discussed in Section **??**.

As detailed in Appendix B, the standard deviation of energy measurements is calculated using the `calculate_energy_stats` function, providing both average energy and standard deviation. This statistical approach offers a visual representation of measurement variability through error bars. The use of standard deviation in mass spectrometry is well-documented in scientific literature. For instance, standard deviation is commonly used to represent uncertainties in measurements and to describe the scatter among measured data points [6]. This statistical approach is crucial for characterizing data variability and ensuring the accuracy of the measurements.

3.5.2 QCM and Ion Current Probe Measurements

For the ion current probe measurements, the standard deviation of the averaged measurements is calculated to characterize the variability in the data. This variability within a pulse can be attributed to several factors, including fluctuations in the plasma potential at the beginning of the pulse, charge exchange reactions between ions and neutrals, and variations in the arc current and pulse parameters. These factors can cause fluctuations in the ion current during the pulse, leading to the observed variability [3]. This kind of instability within the pulse will be henceforth shown with the help of error bars.

However, certain sources of error specific to the ion probe must be considered. The design of the ion probe can influence the measurements due to sheath effects, where the sheath around the probe can expand based on the probe's size and the biasing applied [2, Appendix A.2]. Additionally, secondary electron emissions from the probe surface can affect the ion current measurements [2, Chap. 8.2]. These emissions can be caused by interactions between the ions and the probe surface, leading to inaccuracies in the measurements. As stated before, each pulse varies in terms of energies and amount of particles; these variations are investigated briefly in Sec. 4.1.4, but cannot be considered for every data point.

The QCM measurements are subject to inaccuracies in terms of the error in the resonance frequency measurements, which is based on the manufacturer's specifications. The given measurement inaccuracy is $\Delta f = 0.03$ Hz, which will be taken for error propagation [14]. Additionally, the relative position of the QCM sensor with respect to the ion flux can affect the accuracy of the measurements. The mass deposition rate

is determined from the frequency shift according to the Sauerbrey equation [22], and subsequent calculations of mass flux depend on the measurement duration and sensor area.

3.5.3 Error Propagation Analysis

To properly characterize the uncertainties in the derived quantities, a comprehensive error propagation analysis was performed. The primary measured quantities with associated uncertainties are: the ion current I_{ion} with standard deviation σ_I, the deposited mass m measured by QCM with uncertainty σ_m, and the mean charge state $\bar{Q}$ with standard deviation σ_Q determined from mass spectrometry measurements. These independent measurements are combined to calculate particle fluxes, necessitating careful propagation of uncertainties through the calculation chain.

Ion Flux from Current Measurements

The ion flux in mass units Φ_{ion} (in μg/cm^2/s) is calculated from the measured ion current according to:

$$\Phi_{\text{ion}} = \frac{I_{\text{ion}} \cdot M_{\text{eff}}}{\bar{Q} \cdot e \cdot A} \tag{3.12}$$

where $M_{\text{eff}} = \sum_i f_i \cdot M_i$ is the effective molar mass determined from the species composition measured by mass spectrometry, with f_i being the relative fraction of species i (Al, Ti, N, N_2) and M_i the corresponding atomic or molecular mass. Here $e = 1.602 \times 10^{-19}$ C is the elementary charge and A is the collection area of the ion probe.

For error propagation, considering the independent uncertainties in I_{ion}, $\bar{Q}$, and M_{eff}, the standard Gaussian error propagation formula gives [23]:

$$\left(\frac{\sigma_{\Phi_{\text{ion}}}}{\Phi_{\text{ion}}}\right)^2 = \left(\frac{\sigma_I}{I_{\text{ion}}}\right)^2 + \left(\frac{\sigma_Q}{\bar{Q}}\right)^2 + \left(\frac{\sigma_{M_{\text{eff}}}}{M_{\text{eff}}}\right)^2 \tag{3.13}$$

This shows that the relative uncertainties add in quadrature, which is typical for multiplicative error propagation. The uncertainty in M_{eff} arises from the variability in species fractions and individual charge states measured by mass spectrometry.

Atomic Flux from QCM Measurements

The atomic flux Φ_{atom} (in atoms/cm^2/s) is determined from the mass flux measured by the QCM:

$$\Phi_{\text{atom}} = \frac{\Phi_{\text{mass}} \cdot N_A}{M_{\text{eff}}} \tag{3.14}$$

where $\Phi_{\text{mass}} = m/(A_{\text{QCM}} \cdot t)$ is the mass flux and $N_A = 6.022 \times 10^{23}$ mol^{-1} is Avogadro's constant. Following the same approach:

$$\left(\frac{\sigma_{\Phi_{\text{atom}}}}{\Phi_{\text{atom}}}\right)^2 = \left(\frac{\sigma_m}{m}\right)^2 + \left(\frac{\sigma_{M_{\text{eff}}}}{M_{\text{eff}}}\right)^2 \tag{3.15}$$

The QCM mass uncertainty σ_m is calculated from the frequency measurement uncertainty $\Delta f = 0.03$ Hz using the Sauerbrey relation.

Ion Flux in Atomic Units

To enable direct comparison between ion current and QCM measurements, the ion flux is also expressed in atomic units:

$$\Phi_{\text{ion,atoms}} = \frac{\Phi_{\text{ion}} \cdot N_A}{M_{\text{eff}}} \tag{3.16}$$

The relative uncertainty follows from combining Eqs. (3.13) and the transformation:

$$\left(\frac{\sigma_{\Phi_{\text{ion,atoms}}}}{\Phi_{\text{ion,atoms}}}\right)^2 = \left(\frac{\sigma_I}{I_{\text{ion}}}\right)^2 + \left(\frac{\sigma_Q}{\bar{Q}}\right)^2 + 2\left(\frac{\sigma_{M_{\text{eff}}}}{M_{\text{eff}}}\right)^2 \tag{3.17}$$

Note the factor of 2 for the effective molar mass uncertainty, since M_{eff} appears in both the ion flux calculation and the unit conversion.

Results

4.1 Langmuir Probe Bias Voltage Characterization

4.1.1 Validation of Langmuir Probe Operation

Before plasma diagnostics were performed, the functionality of the custom-built Langmuir probe was verified by checking the characteristic voltage current curve (I-V curve) and fitting it against the theoretical relationship 4.1. Additionally the appropriate negative bias voltage for ion saturation measurements was determined . The goal was to ensure that the probe operates in a regime where the collected current is dominated by ions, excluding contributions from electrons.

The bias voltage tests were performed without nitrogen in the chamber, at a fixed distance of 10 cm from the macroparticle filter, and with an EM coil strength of 0.25 T. Figure 4.1 displays the measured ion current as a function of bias voltage. The blue data points represent the experimental results, while the green line shows the exponential saturation fit.

The relationship between the collected current I and the bias voltage V was analyzed using the modified Langmuir equation [7]:

$$I = I_{\text{sat}} \left(1 - e^{\frac{-V}{V_0}} \right) + m \cdot V \tag{4.1}$$

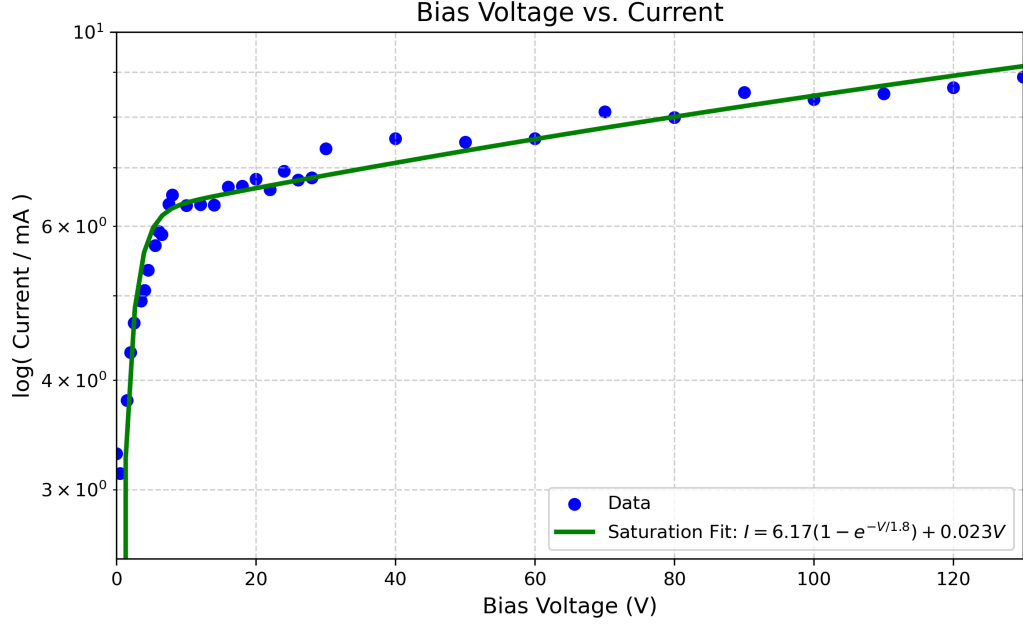where I_{sat} is the saturation current and V_0 is a characteristic voltage. The term k

Figure 4.1: Measured ion current vs. bias voltage for the Langmuir probe, showing exponential saturation fit $I = 6.17(1 - e^{-V/1.8}) + 0.023V$. Conditions: no nitrogen, 10 cm from the macroparticle filter, 0.25 T EM-coil strength.

in the equation accounts for plasma sheath expansion and collisional effects at higher bias voltages.

4.1.2 Analysis of the Ion Saturation Curve

As the bias voltage increases, the sheath around the probe grows, which can lead to a non-saturating component in the collected current, this is a common effect seen in small probes. Additionally, collisions within the sheath or presheath region can modify the ion trajectory, resulting in a small linear increase in the collected current with voltage. This correction ensures the model accurately describes the probe's behavior across the full range of applied voltages [7, Chap. 7].

The experimental data were fitted to this equation using a nonlinear least-squares method in Python, yielding the following parameters:

$$I_{sat} = 6.17\,\text{mA}, \qquad V_0 = 1.8\,\text{V}, \qquad k = 0.023.$$

The bias voltage test results (Figure 4.1) show two distinct regimes:

1. **Transition Regime ($0 - 40$ V):**
   At low bias voltages, the probe collects both ions and electrons. As the negative bias increases, more electrons are repelled, reducing their contribution to the

27

measured current. This results in a rapid rise in net current as the ion flux begins to dominate. The transition regime is characterized by a balance between the decreasing electron flux and the increasing ion flux.

2. **Saturation Regime (40 − 130V):**
Beyond approximately 40V, the current plateaus, indicating that the probe has entered the ion saturation regime. At this point, the negative bias effectively repels all electrons, and the collected current is dominated by ions. However, the current increases slightly with voltage, which is captured by the linear correction term $k = 0.023$ in the modified Langmuir equation.

4.1.3 Selection of Operating Bias Voltage

A bias voltage of -80 V was selected for subsequent measurements to ensure the probe operates well within the ion saturation regime. While the curve begins to saturate around 40 V, choosing a higher voltage provides confidence that the probe is fully repelling electrons and measuring ion flux reliably.

4.1.4 Ion current probe Errors

4.2 Quartz crystal Microbalance and Ion current Probe

Although the measurements were taken at the same time and location, the results will be presented in two subsections for clarity: first, the Quartz Crystal Microbalance (QCM) data, followed by the Ion Current Probe results. This structure is intended to improve the readability and understanding of the trends.
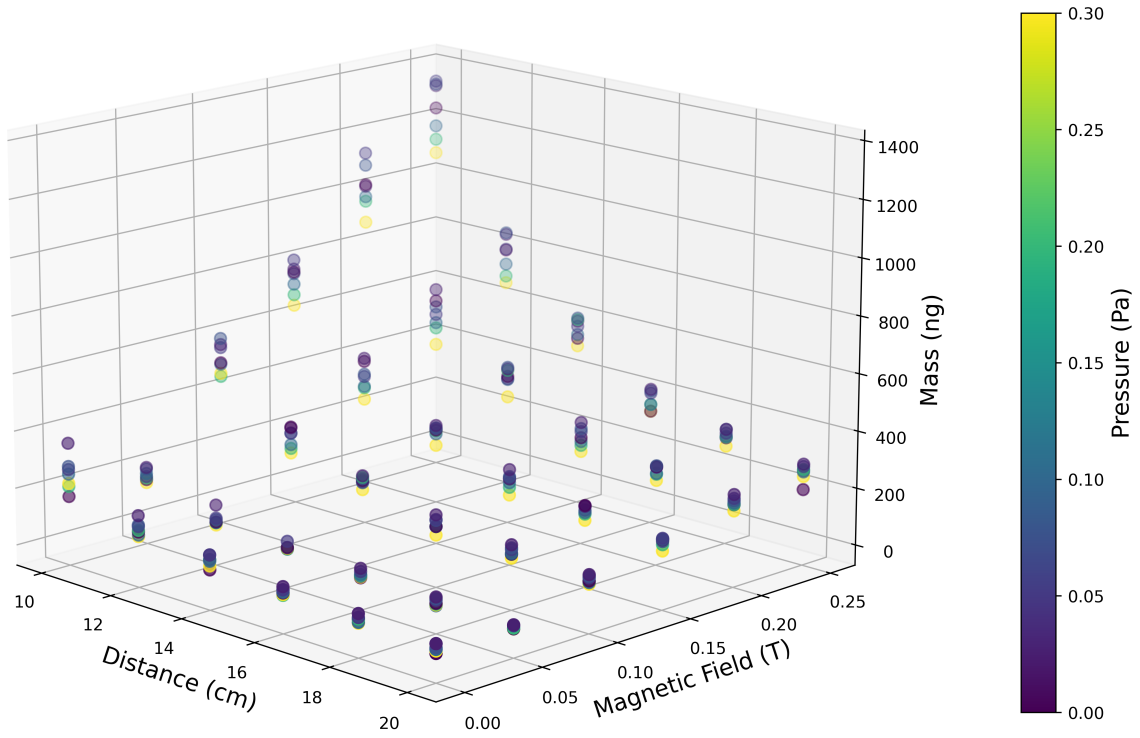
Distance (cm)	Pressure (Pa)	Magnetic Field (T)
10	0	0
12	0.025	0.05
14	0.05	0.1
16	0.075	0.15
18	0.1	0.2
20	0.2	0.25
	0.3	

Table 4.1: Parameters used for the QCM/ Ion current probe

In Figures 4.2a and 4.2b, a complete overview of the dataset of the measured ion currents and the deposited masses depending on three parameters are shown. These
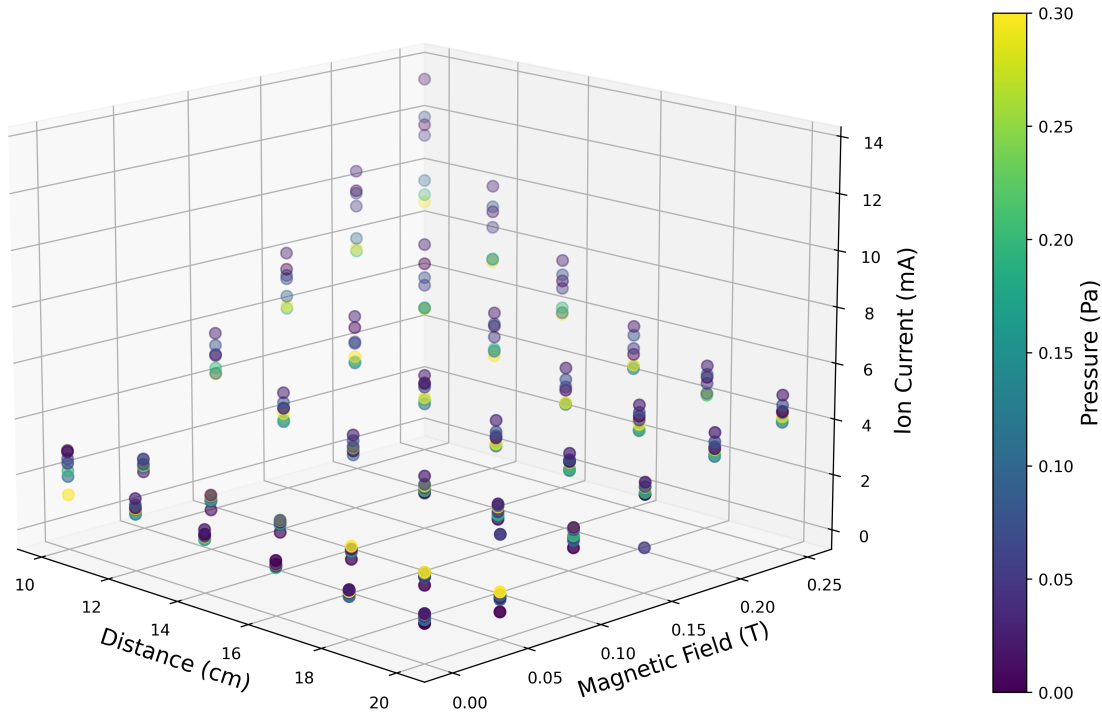
are the distance to the macroparticle filter, the magnetic field strength and the nitrogen background pressure in the chamber. Data points for 0 Pa are in reality more in the order of $1.5 \cdot 10^{-5}$ Pa.

Mass (ng) vs. Distance (cm), Magnetic Field (T) and Pressure (Pa)

(a)

Ion Current (mA) vs. Distance (cm), Magnetic Field (T) and Pressure (Pa)

(b)

Figure 4.2: (a) The deposited mass (b) The ion current vs. distance, magnetic field strength, and nitrogen background pressure over 64 pulses. Conditions: nitrogen background pressure from 0 Pa to 0.3 Pa, distance from 10 cm to 20 cm from the macroparticle filter, and magnetic field strength from 0 T to 0.25 T.
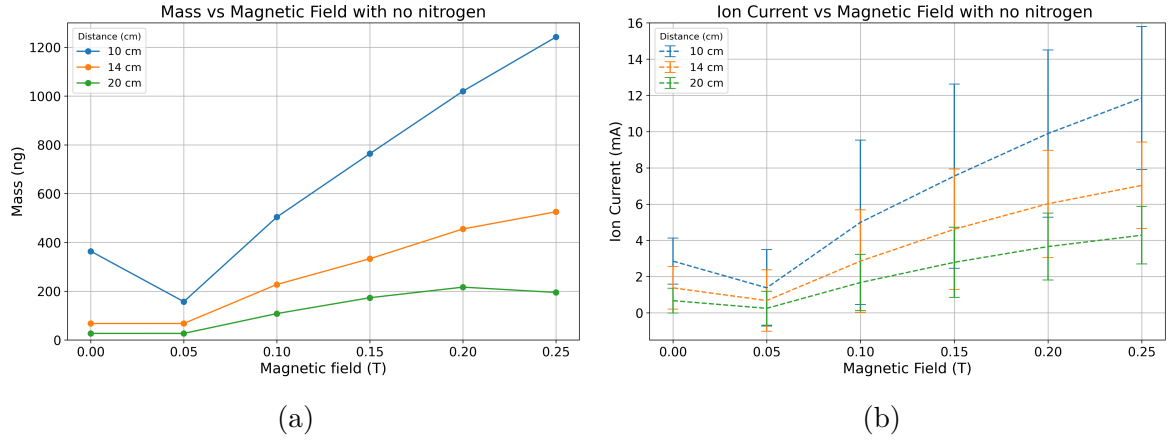
Figure 4.3: yeah dunno (a) mass and (b) ion current

General trends that can be seen already in these figure include:

- The deposited mass and ion current decreases as the distance from the macroparticle filter increases (see Section 4.2.2).

- Higher magnetic field strengths tend to increase the deposited mass and the ion current (see Section 4.2.3).

- The deposited mass shows a complex dependence on nitrogen background pressure. Whereas the ion current seems to be decreasing with increasing nitrogen contents(see Section 4.2.4).

This overview sets the stage for a more detailed analysis of each variable's impact on the deposited mass and ion current. In the following subchapters, we will first examine the metallic case (no nitrogen) with respect to distance and magnetic field strength. Then, we will focus on the specific effects of distance (10 cm, 14 cm, and 20 cm), magnetic field strength (0 T, 0.15 T, and 0.25 T), and nitrogen background pressure (0.1 Pa, and 0.3 Pa) as these are the parameters, which are looked at in more detail with the help of

4.2.1 Metallic Case (No Nitrogen)

In this section, we analyze the deposited mass as a function of distance and magnetic field strength in the absence of nitrogen.

4.2.2 Distance as a variable

4.2.3 Magnetic field as a variable

4.2.4 Nitrogen pressure as a variable
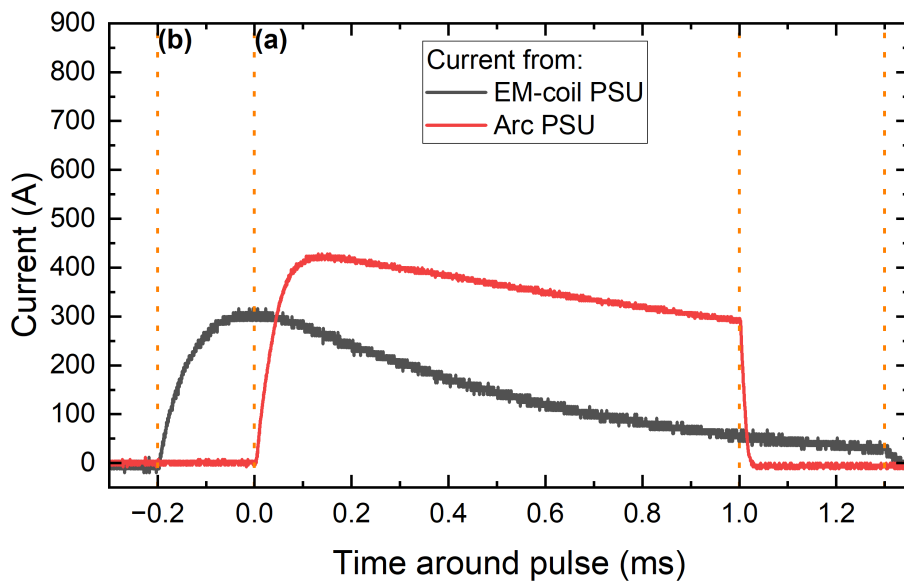
APPENDIX A

Additional Plots

Figure A.1: Additional Pulse waveform with the triggering timings (a) and (b) for the Arc-PSU and the EM-coil PSU marked with the orange dashed line for 100V input

APPENDIX B

Python code used

Bibliography

[1] Hiden Analytical. EQP: Mass and Energy Analyser for plasma diagnostics. https://www.hidenanalytical.com/wp-content/uploads/2016/08/EQP-poster_A1_print.pdf, 2016. [Accessed 18-11-2025].

[2] André Anders. *Cathodic arcs: from fractal spots to energetic condensation*, volume 50. Springer, 2008.

[3] André Anders. The evolution of ion charge states in cathodic vacuum arc plasmas: a review. *Plasma Sources Science and Technology*, 2012. A review article that discusses various factors influencing ion charge states in cathodic vacuum arc plasmas.

[4] André Anders and George Yu Yushkov. Ion flux from vacuum arc cathode spots in the absence and presence of a magnetic field. *Journal of Applied Physics*, 91(8):4824–4832, 2002.

[5] J. Benedikt et al. Quadrupole mass spectrometry of reactive plasmas. *Surface & Coatings Technology*, 206:579–588, 2012.

[6] R. L. Boxman, S. Goldsmith, and D. M. Sanders. Cathodic arc plasmas and their applications. *IEEE Transactions on Plasma Science*, 23(6):939–956, 1995. Includes quantitative plasma diagnostics where standard deviation is used to characterize measurement scatter and reproducibility of arc plasma parameters.

[7] Francis F. Chen. *Introduction to Plasma Physics and Controlled Fusion*, volume 1. Springer, New York, 1984.

[8] Jean Daillant and Alain Gibaud. *X-ray and Neutron Reflectivity: Principles and Applications*, volume 770 of *Lecture Notes in Physics*. Springer, Berlin, 2009.

[9] P. H. Dawson. *Quadrupole Mass Spectrometry and Its Applications.* IM Publications, Chichester, UK, 1997.

[10] Joseph I. Goldstein, Dale E. Newbury, Joseph R. Michael, Nicholas W. M. Ritchie, John Henry J. Scott, and David C. Joy. *Scanning Electron Microscopy and X-Ray Microanalysis.* Springer, New York, 4th edition, 2017.

[11] Hiden Analytical, Warrington, UK. *EQP Technical Manual: Energy-Resolving Quadrupole Mass Spectrometer*, 2024.

[12] V. Holý, U. Pietsch, and T. Baumbach. *High-Resolution X-Ray Scattering from Thin Films and Multilayers*, volume 149 of *Springer Tracts in Modern Physics.* Springer, Berlin, 1999.

[13] A. Hubaux and G. Vos. Quantitative mass spectrometry: Part ii. *Anal. Chem.*, 42(8):849, 1970.

[14] INFICON, Bad Ragaz, Switzerland. *SQM-160 Multi-Film Rate/Thickness Monitor Operating Manual*, 2015. PN 074-511-P1E.

[15] H. Kiessig. Interferenz von Röntgenstrahlen an dünnen Schichten. *Annalen der Physik*, 402(7):769–788, 1931.

[16] C. Lu and O. Lewis. Investigation of film-thickness determination by oscillating quartz resonators with large mass load. *Journal of Applied Physics*, 43(11):4385–4390, 1972.

[17] R. E. March and R. J. Hughes. *Quadrupole Storage Mass Spectrometry.* Wiley, 1989.

[18] R. E. Miller and D. I. Bolef. Shear modulus and internal friction in single-crystal quartz at low temperatures. *Journal of Applied Physics*, 39(11):5815–5821, 1968.

[19] L. G. Parratt. Surface studies of solids by total reflection of x-rays. *Physical Review*, 95(2):359–369, 1954.

[20] C. Y. Poon and B. Bhushan. *Comparison of surface roughness measurements by stylus profiler, AFM and non-contact optical profiler*, volume 190. 1995.

[21] Ludwig Reimer. *Scanning Electron Microscopy: Physics of Image Formation and Microanalysis*, volume 45 of *Springer Series in Optical Sciences.* Springer, Berlin, 2nd edition, 1998.

[22] Günter Sauerbrey. Verwendung von schwingquarzen zur wägung dünner schichten und zur mikrowägung. *Zeitschrift für Physik*, 155(2):206–222, Apr 1959.

[23] John R. Taylor. *An Introduction to Error Analysis: The Study of Uncertainties in Physical Measurements.* University Science Books, Sausalito, CA, 2nd edition, 1997.

[24] Metin Tolan. *X-Ray Scattering from Soft-Matter Thin Films: Materials Science and Basic Research*, volume 148 of *Springer Tracts in Modern Physics.* Springer, Berlin, 1999.

[25] Yeliz Unutulmazsoy, Dmitry Kalanov, Kyunghwan Oh, Soheil Karimi Aghda, Jürgen W. Gerlach, Nils Braun, Frans Munnik, Andriy Lotnyk, Jochen M. Schneider, and André Anders. Toward decoupling the effects of kinetic and potential ion energies: Ion flux dependent structural properties of thin (v,al)n films deposited by pulsed filtered cathodic arc. *Journal of Vacuum Science & Technology A*, 41(6), 2023.

[26] David B. Williams and C. Barry Carter. *Transmission Electron Microscopy: A Textbook for Materials Science.* Springer, New York, 2nd edition, 2009.

[27] D. Windover, K. M. Gaff, D. Lee, and M. J. Dalberth. Profilometry and atomic force microscopy for surface characterization. *Materials Characterization*, 43(5):347–355, 1999.